Supporting Information

Mechanism for spiral growth of β-antimonene on a pitted substrate: vacancy line aggregation triggered by nano-scale step-loops

Wenmin Li[a], Hao Hu[b*], Yi Pan[a*]

[a] Center for Spintronics and Quantum Systems, State Key Laboratory for Mechanical Behavior of Materials, Xi'an Jiaotong University, Xi'an 710049, China

[b] Luology(Shandong) Digital Technology Co., LTD., Weifang 261021, China

***Email:** hao_hu@luology.com; yi.pan@xjtu.edu.cn

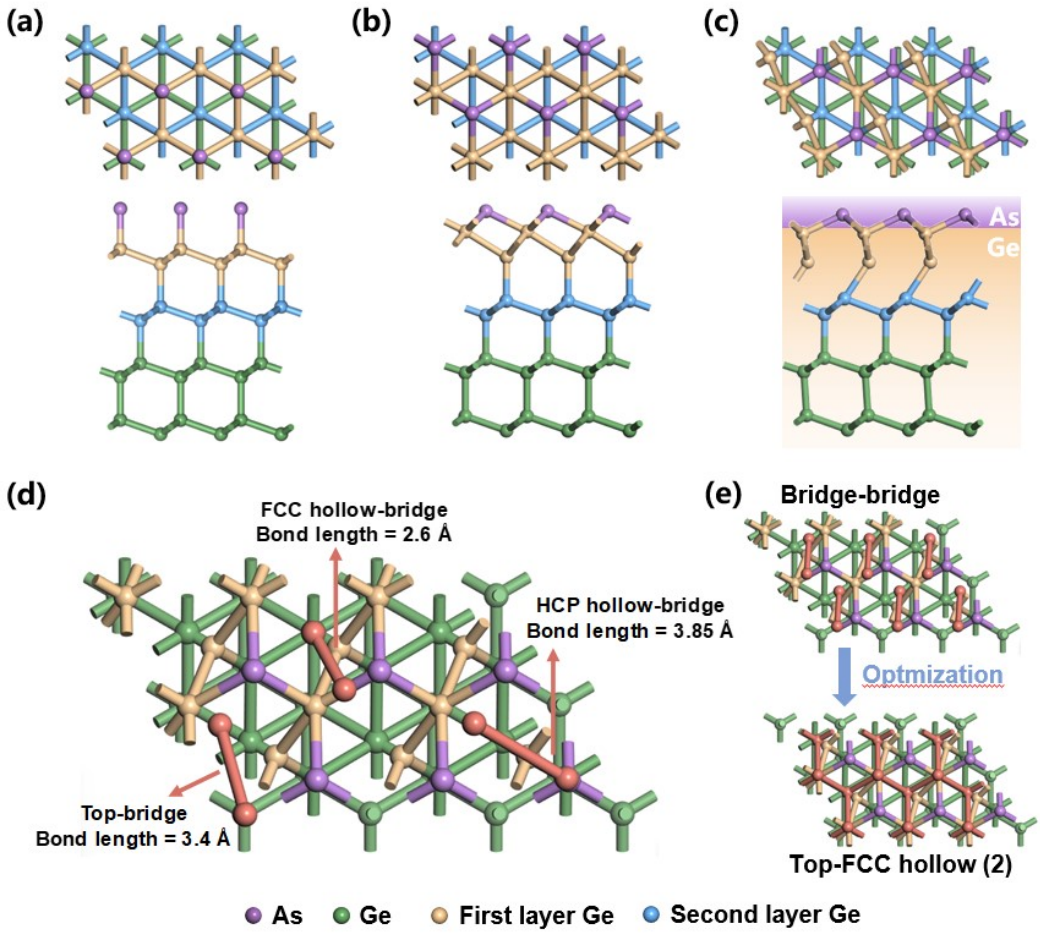

Fig. S1 (a) The optimized structure of As atom adsorbed on the top site. (b) The optimized structure of As atom adsorbed on the FCC hollow site. (c) The most stable adsorption configuration: the optimized structure of As atom adsorbed at bridge site and HCP hollow site. (d) The possible configurations and bond lengths of β-Sb at the bridge sites and top, FCC hollow, and HCP hollow sites on the Ge(111) substrate surface. (e) Structure of optimization of β-Sb on the bridge-bridge of As/Ge(111) surface.

Table S1 Energies of As atoms at different sites on Ge(111) and adsorption energies of antimonene at different sites on As/Ge substrates

As/Ge	$E_{sub(As+Ge(111))}$	Antimonene-As/Ge structures	E_{total}	E_{ad}
Bridge	-40.7729	Top-FCC hollow	-49.8783	-0.5346
		Top-FCC hollow (2)	-50.0421	-0.6984
		Top-HCP hollow	-49.9864	-0.6427
		Top-HCP hollow (2)	-50.0404	-0.6967
		FCC hollow-HCP hollow	-49.9029	-0.5592
		FCC hollow-HCP hollow (2)	-50.0436	-0.6999
		Bridge-bridge	-50.0407	-0.6970
FCC hollow	-40.4646	——	——	——
HCP hollow	-40.7728	——	——	——
Top	-40.4231	——	——	——

The bridge-bridge configuration, after optimization, also forms the most stable top-FCC hollow (2) structure (Fig. S1e), with an energy difference of approximately 0.0014 eV, which can be considered negligible. The large atomic optimization displacement further confirms the instability of the antimonene structure at the bridge-bridge site.

Table S2 The formation energy of vacancies of monolayer 7 × 7 β-antimonene under two kinds of strains

n	n vacancies	ε ≈ 7.07 % $E_{n\ vcacy}$ (eV)	ε ≈ 3 % $E_{n\ vancy}$ (eV)
1	A	1.6473	2.1754
	AB_1	1.7331	2.5367
	AB_2	1.8934	2.7477
2	AB_3	2.0425	2.9536
	AB_4	2.5490	3.4993
	AB_5	2.7216	3.6999
	AB_1C_1	3.2905	4.0189
3	AB_1C_2	2.7227	3.6422
	AB_1C_3	3.1846	4.4869
	$AB_1C_2D_1$	3.4467	4.4410
	$AB_1C_2D_2$	4.2829	4.6229
4	$AB_1C_2D_3$	3.4470	4.4432
	$AB_1C_2D_4$	2.5897	4.0316
	$AB_1C_2D_4E_1$	3.749397	5.0669
	$AB_1C_2D_4E_2$	4.288644	5.1894
5	$AB_1C_2D_4E_3$	3.749428	5.0671
	$AB_1C_2D_4E_4$	4.123952	6.0187
	$AB_1C_2D_4E_3F_1$	3.9377	5.7612
	$AB_1C_2D_4E_3F_2$	5.0255	5.7913
6	$AB_1C_2D_4E_3F_3$	4.3774	5.7412
	$AB_1C_2D_4E_3F_4$	4.7252	5.4291

	7.07% conpressive strain	3% conpressive strain
Single vacancy_A	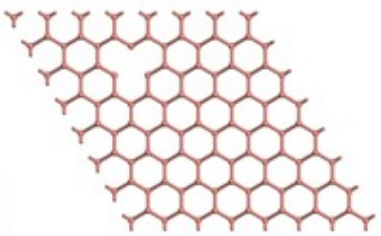	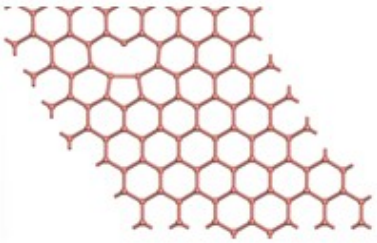
Double vacancy_AB_1	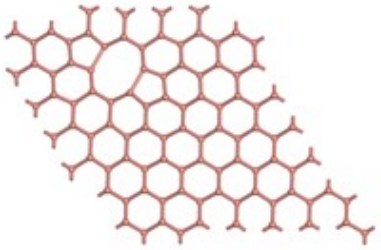	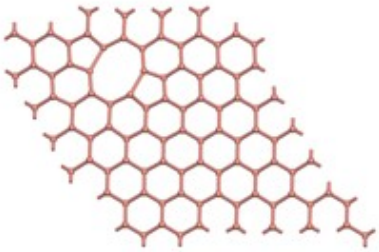
Double vacancy_AB_2	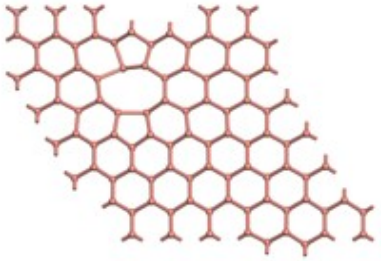	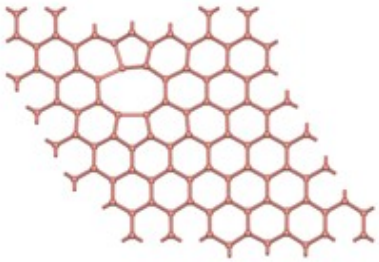
Double vacancy_AB_3	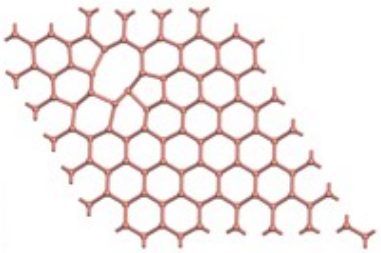	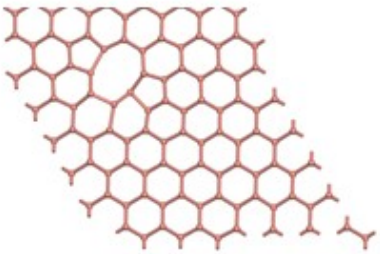
Double vacancy_AB_4	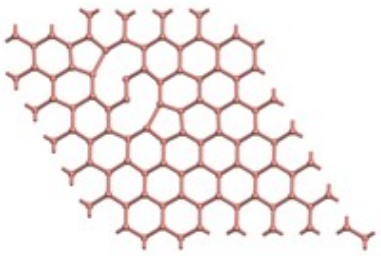	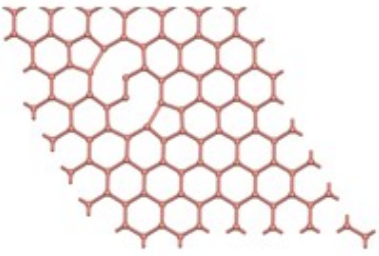

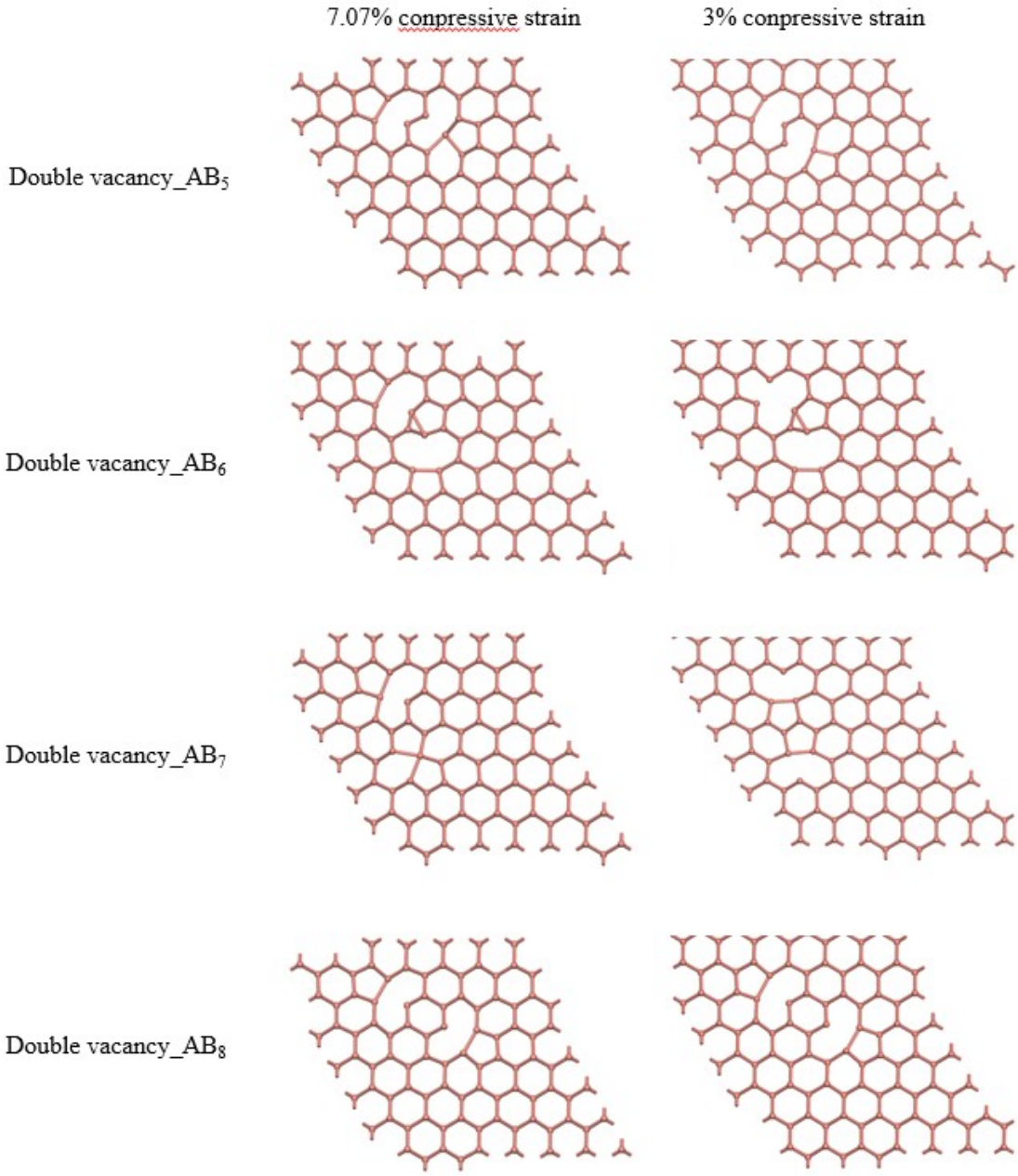

Fig. S2 Comparison of optimized structures of single vacancy and eight double vacancies of β-antimonene under two strains.

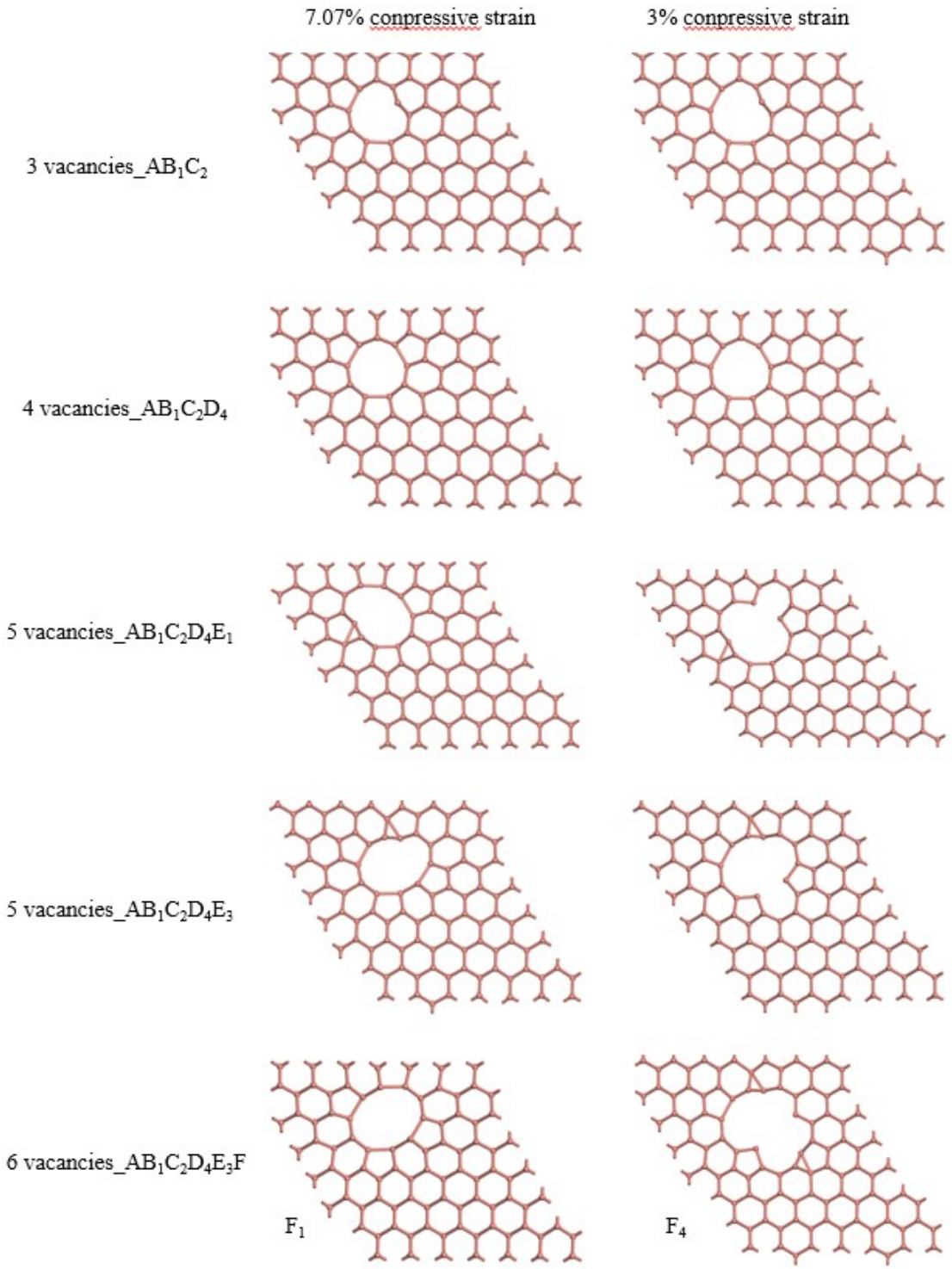

Fig. S3 Comparison of the most stable configurations from tri-vacancies to hexa-vacancies of β-antimonene under two strains.

When calculating the four configurations of penta-vacancy, $AB_1C_2D_4E_1$ and $AB_1C_2D_4E_3$ exhibit the same energy under two different strain conditions, as shown in Table S2. Additionally, their optimized structures are identical (as depicted in the Fig.

S3). We chose one of them, $AB_1C_2D_4E_3$, as the basis for studying hexa-vacancy. It is evident that the configurations of penta-vacancy conform to the conclusion that vacancies tend to aggregate.

Table S3 Spin-polarized energy of As/Ge(111) and antimonene-As/Ge(111)

As/Ge	E (eV)	E (eV) (Spin polarization)	Antimonene-As/Ge	E_{ad} (eV)	E_{ad} (eV) (Spin polarization)
Bridge	-40.7729	-40.7938	Top-FCC hollow (2)	-0.6984	-0.717
FCC hollow	-40.4646	-40.4849	———	———	———
HCP hollow	-40.7728	-40.7963	———	———	———
Top	-40.4231	-40.4544	———	———	———

Table S4 Energy of six vacancies under two different strains

n	strain	n vacancies	$E_{n\ vcacy}$ (eV)	$E_{n\ vancy}$ (eV) (Spin polarization)
6	ε = 7.07 %	$AB_1C_2D_4E_3F_1$	3.9376	3.9375
	ε = 3 %	$AB_1C_2D_4E_3F_1$	5.7612	5.6757
		$AB_1C_2D_4E_3F_2$	5.7913	5.6272
		$AB_1C_2D_4E_3F_3$	5.7412	5.5589
		$AB_1C_2D_4E_3F_4$	5.4291	5.2049

The effects of spin-orbit coupling (SOC) have not been considered in the interface engineering and strain engineering studies of antimonene[1-3] and in the vacancy studies of phosphorene[4, 5]. However, SOC is often incorporated in studies of the magnetic properties of materials[6, 7]. In the Sb/As/Ge system, non-magnetic materials show weak SOC effects. Nevertheless, spin-related effects may emerge due to defects, heterojunctions, and the adsorption sites of surface atoms.

The spin polarization at the Ge(111) adsorption sites and heterojunctions of Sb/As/Ge(111) introduces a minor energy shift of 0.02 eV. The energy of the six vacancies in antimonene is almost unaffected by spin polarization under large strain, while the spin-polarized energy contribution under small strain ranges from 0.09 to 0.17 eV. However, this does not alter our conclusion: the formation energy of vacancies under large strain is lower than that of vacancies under small strain, and the hexa-vacancy structure $AB_1C_2D_4E_3F_4$ is the most stable under small strain.

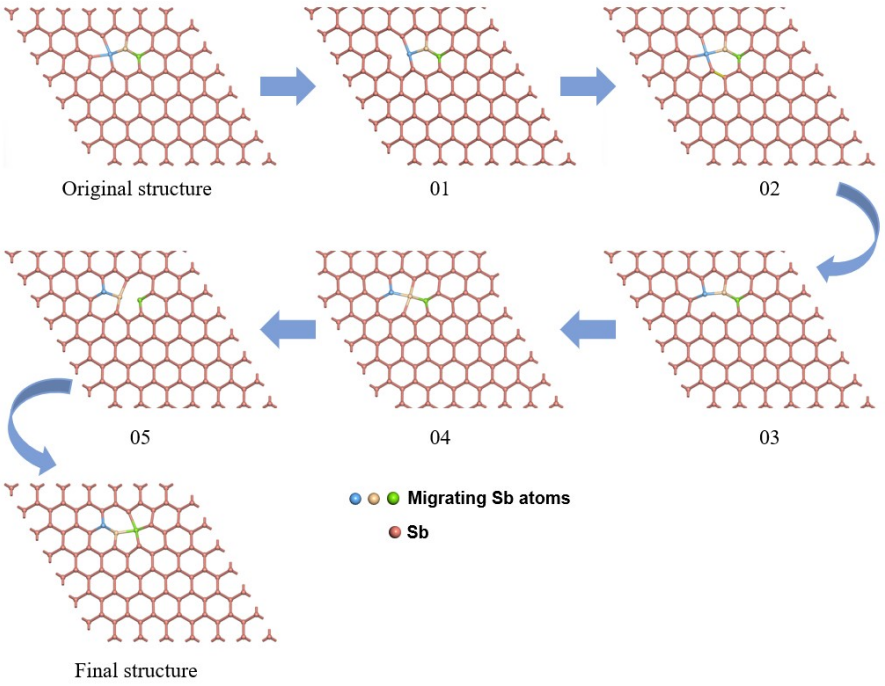

Fig. S4 Structural changes in the transition state of the single vacancy migration of β-antimonene under 7.70% compressive strain.

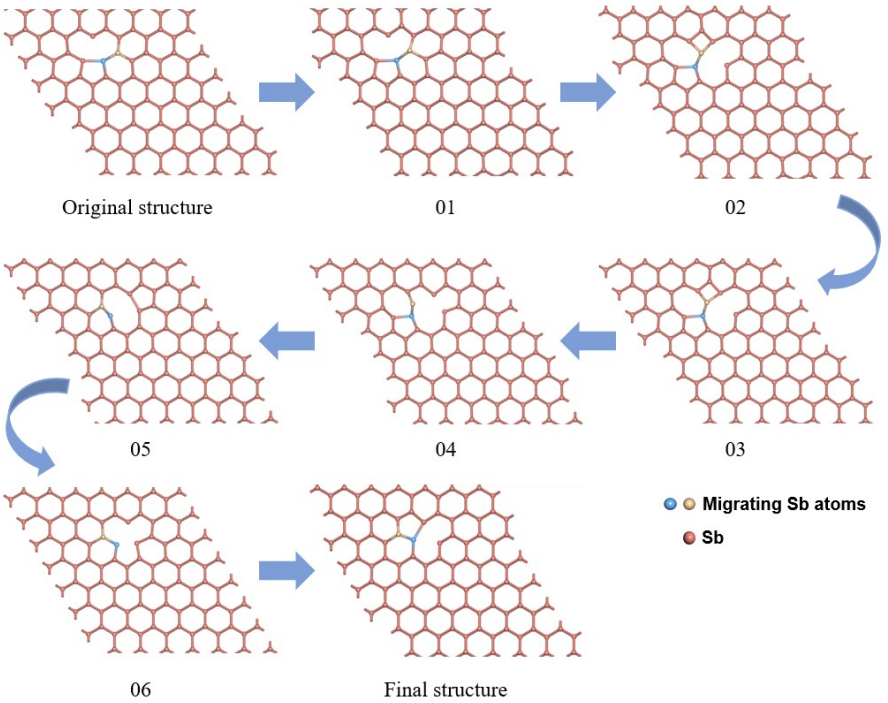

Fig. S5 Structural changes in the transition state of the single vacancy migration of β-antimonene under 3% compressive strain.

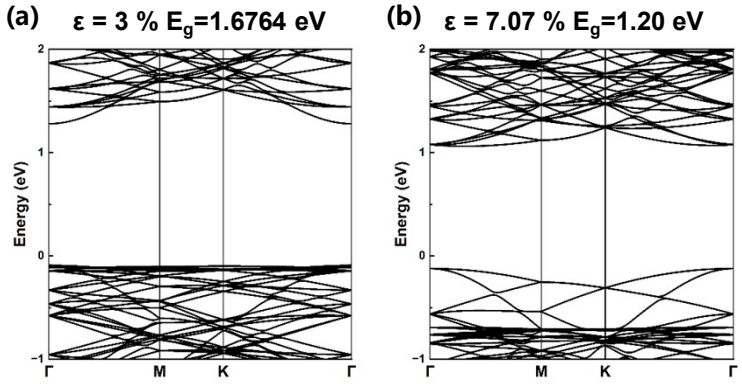

Fig. S6 Band structures of Sb under (a) 3% compressive strain and (b) 7.07% compressive strain.

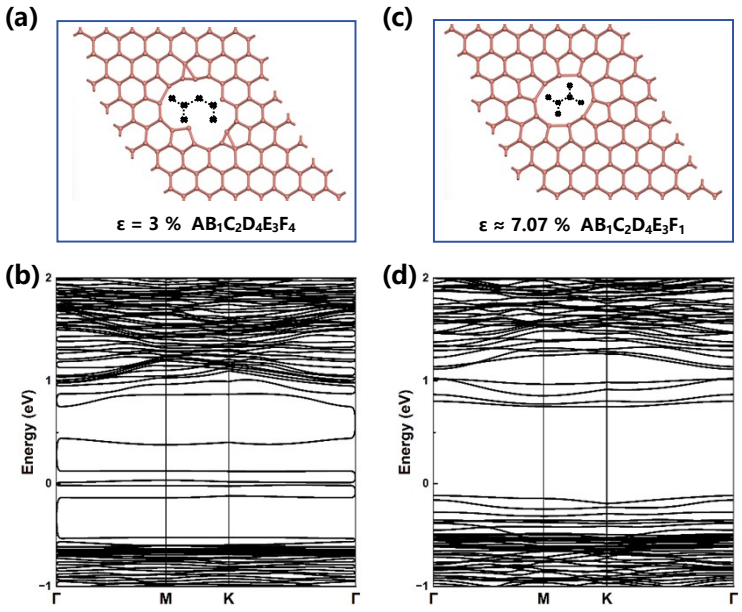

Fig. S7 The (a) atomic structures and (b) band structure of Sb with irregular vacancy defects. The (c) atomic structures and (d) band structure of Sb with regular vacancy defects.

As shown in Fig. S6, antimonene under large compressive strain in step loops exhibits a reduced bandgap of 1.2 eV, smaller than the 1.6764 eV bandgap in small compressive strain, consistent with previous strain-bandgap relationships[7].

As shown in Fig. S7, Irregular vacancy defects induce near-zero bandgap states (0.02 eV) in Sb, suggesting potential metallic/semimetallic behavior. Regular hexa-vacancy defects retain semiconducting properties with a 0.9182 eV bandgap, corroborating earlier reports that single vacancies induce metallicity while divacancies

preserve semiconductor characteristics[6].

Furthermore, the strongly strained antimonene displays flat bands and pronounced electron localization in its band structure, indicating that the spiral-structured semiconductor possesses unique electrical properties distinct from conventional forms (Fig. S2b).

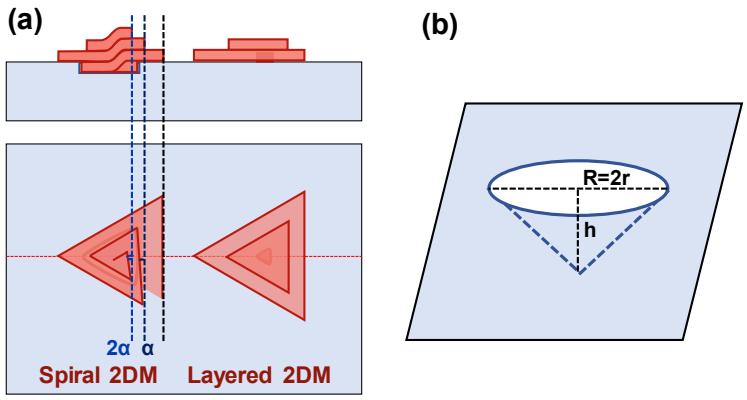

Fig. S8 (a) The materials with different structures grown on substrates. (b) Schematic diagram of depressions curvature on the substrate surface.

In this work, the accumulated lattice strain in the step loops is identified as the key factor for spiral formation. The twisted angle of the spiral structure is closely linked to the size and height of the step loops. This is consistent with the experimental observations[8]: The variation in moiré periods (7 to 10 nm) and twist angles (2.3° to 3.3°) may result from the random sizes of 'step loops' on the substrate.

We propose a theoretical growth model of twisted spiral structures based on the nanoscale step loops on the substrate. Using DFT, we have demonstrated the formation of screw dislocations under large compressive strain within step loops. The twisted angle of the spiral structure depends on the configuration of the step loops, with smaller radii and deeper depressions corresponding to higher curvatures to form fastened supertwisted spiral,[9] as shown in Fig. S8.

Note：The interlayer twist is not governed by the Eshelby twist mechanism

In the twisted spiral Sb experiment report, the single-layer step loops (with a height of 4 Å and a diameter of 50-100 nm) display small curvature, leading to lower twist angles in the resulting spirals (2.3° to 3.3°). Such interlayer twist is not governed by the Eshelby twist mechanism. The following analysis and discussion, supported by theoretical calculations and experimental observations, substantiate this argument.

1. Theoretical Exclusion of Eshelby Twist Dominance

The Eshelby twist angle, derived from the classical formula[10, 11]:

$$\alpha = \frac{b}{\pi r^2}$$

For spiral antimonene: Burgers vector b ≈ 4.12 Å (aligned with the theoretical value of lattice constant of free-standing antimonene[8]); Lateral radius r ≈ 50 nm (R=2r=100 nm as lateral size of the spirals measured experimentally[8]). Substituting these values:

$$\alpha \approx \frac{0.412\ nm}{\pi \times (50\ nm)^2} \approx 5.247 \times 10^{-5} rad/nm\ (\sim 0.003007°/nm)$$

This calculated angle is three orders of magnitude smaller than the observed interlayer twist angles (2.3°–3.3°), strongly ruling out Eshelby twist as the primary mechanism.

2. Experimental Evidence Against Eshelby Twist

2.1. Key observations further exclude Eshelby-driven effects:

Absence of Cumulative Twisting: The interlayer angles induced by the Eshelby twist would theoretically accumulate with increasing layer numbers. However, in the experimentally observed spiral structures, which exhibit well-defined twist angles of 2.3°–3.3° with an average thickness of 10 atomic layers (The single atomic layer of antimonene is approximately 4 Å), these characteristic angles cannot be attributed to layer-by-layer angular accumulation.

Size Independence: Eshelby twist angles decay rapidly with lateral size ($\alpha \propto 1/r^2$). For our large spirals (R = 2r ≈100 nm), Eshelby contributions would be negligible, yet the observed twist angles remain significant.

2.2. Direct Correlations Between Strain and Electronic Properties

The STM and spectroscopy data further support a substrate-driven mechanism:

Strain Pinning: The helical dislocation acts as a pinning center for anisotropic strain[8], which modifies electronic states and work function. These effects are tied to geometric distortions rather than Eshelby shear.

Tip-Induced Strain Manipulation: Reversible tuning of interlayer coupling via STM tip pressing demonstrates that strain, and thus the twist angle, is externally controllable, a feature incompatible with intrinsic Eshelby mechanics.

References

1. K.-X. Chen, S.-S. Lyu, X.-M. Wang, Y.-X. Fu, Y. Heng and D.-C. Mo, *The Journal of Physical Chemistry C*, 2017, **121**, 13035-13042.
2. T. Niu, W. Zhou, D. Zhou, X. Hu, S. Zhang, K. Zhang, M. Zhou, H. Fuchs and H. Zeng, *Adv Mater*, 2019, **31**, e1902606.
3. Z.-Q. Shi, H. Li, C.-L. Xue, Q.-Q. Yuan, Y.-Y. Lv, Y.-J. Xu, Z.-Y. Jia, L. Gao, Y. Chen, W. Zhu and S.-C. Li, *Nano Letters*, 2020, **20**, 8408-8414.
4. Y. Cai, Q. Ke, G. Zhang, B. I. Yakobson and Y. W. Zhang, *J Am Chem Soc*, 2016, **138**, 10199-10206.
5. M. Peralta, D. A. Freire, R. González-Hernández and F. Mireles, *Physical Review B*, 2024, **110**, 085404.
6. A. Bafekry, M. Ghergherehchi and S. Farjami Shayesteh, *Phys Chem Chem Phys*, 2019, **21**, 10552-10566.
7. D. R. Kripalani, A. A. Kistanov, Y. Cai, M. Xue and K. Zhou, *Physical Review B*, 2018, **98**, 085410.
8. D. M. Huang, X. Wu, K. Chang, H. Hu, Y. L. Wang, H. Q. Xu and J. J. Zhang, *Adv Sci (Weinh)*, 2023, **10**, e2301326.
9. Y. Zhao, C. Zhang, D. D. Kohler, J. M. Scheeler, J. C. Wright, P. M. Voyles and S. Jin, *Science*, 2020, **370**, 442-445.
10. J. D. Eshelby, *Journal of Applied Physics*, 1953, **24**, 176-179.
11. J. Zhu, H. Peng, A. F. Marshall, D. M. Barnett, W. D. Nix and Y. Cui, *Nat Nanotechnol*, 2008, **3**, 477-481.